

Carrier thermalization in sub-three-dimensional electronic systems: Fundamental limits on modulation bandwidth in semiconductor lasers

Igor Vurgaftman, Yeeloy Lam, and Jasprit Singh

*Solid State Electronics Laboratory, Department of Electrical Engineering and Computer Science,
The University of Michigan, Ann Arbor, Michigan 48109-2122*

(Received 31 March 1994)

Carrier equilibration is essential for semiconductor laser operation since carriers are injected into the active region at energies higher than the effective band edges. While the threshold current of the laser diode can be minimized by quantum confinement in extra dimensions, the quantum effects in carrier capture and thermalization become more pronounced. In this paper, a full treatment of the carrier thermalization in electronic systems of reduced dimensionality for injection conditions relevant to laser operation is given based on ensemble Monte Carlo simulations and the fundamental limits on modulation bandwidth are discussed. Results are presented for quantum wells, quantum wires, and quantum dots. The peculiarities of the relaxation process in each structure are elucidated. It is shown that the relaxation times increase from ≈ 1 ps in bulk, to ≈ 10 ps in quantum wells, ≈ 50 ps in quantum wires, and ≈ 200 ps in quantum dots. Since the intraband relaxation times determine the extent of gain nonlinearities in semiconductor lasers, the maximum modulation bandwidth imposed by the intrinsic process of carrier relaxation can be calculated via the dependence of the optical gain on the photon density in the laser structure. For a graded-index quantum-well laser structure, the calculated value of the nonlinear gain coefficient is $1.1 \times 10^{-17} \text{ cm}^3$ with the maximum -3 -dB modulation bandwidth of 78 GHz for a $100\text{-}\mu\text{m}$ cavity length. The nonlinear gain coefficient in quantum wires is enhanced in comparison with quantum wells, although the differential gain may be increased by as much as an order of magnitude with the exact value of the modulation bandwidth dependent on the details of the design of the quantum-wire laser.

I. INTRODUCTION

In recent years, there has been a heightened interest in low-dimensional electronic systems owing to the exciting physics that the structures with quantum confinement of carriers permit us to investigate as well as to the expectation that these structures will form the foundation for qualitatively new classes of electronic and optoelectronic semiconductor devices.¹⁻³ Thus the performance of semiconductor lasers has been found to be beneficially affected by the sharpening of the peak of the electronic density of states near the band edge and symmetrization in the conduction- and valence-band effective masses that simple analysis predicts for progressive reduction in the dimensionality of the carrier states. The anticipation of the transition from bulk and quantum-well active regions to those based on quantum wires and dots with drastic suppression of the threshold currents has generated a considerable amount of research.^{4,5} Considering the potential for highly efficient optoelectronic devices that low-dimensional structures hold, different aspects of laser performance associated with their introduction must be carefully examined.

It is intuitively clear that reduction in the number of final states available for carriers detracts from the efficiency of carrier equilibration by phonon emission. In polar semiconductors, the dominant scattering process responsible for carrier relaxation is polar optical-phonon (POP) emission, the energy loss for which is almost pure-

ly monochromatic owing to the horizontal dispersion of the longitudinal-optical-phonon branch near the zone center. In order to understand better the physics of carrier thermalization relevant to semiconductor lasers, it is important to realize that to ensure a strong overlap between the confined optical mode and the active device region, one has to include a large band-gap cladding layer as shown in Fig. 1(a).^{6,7} The electrons and holes are then injected into the active region as shown. The carriers have energies in excess of $k_B T$ (are "hot") and must lose the excess energy to be available for recombination processes. If carrier thermalization is much faster than the electron-hole recombination rate, the carrier distribution in the active region is given by quasi-Fermi statistics as shown in Fig. 1(b). On the other hand, if the thermalization time is comparable to the recombination time, the carrier distribution remains hot, as shown by the dashed line in Fig. 1(b). Similar considerations are valid for a lower-dimensional active region. As the carriers descend from a three-dimensional (3D) cladding layer into the quantum-confined structure, bottlenecks in carrier relaxation may be created accompanied by a sharp increase in the relaxation time. Furthermore, in quantum wires, the only binary intrasubband electron-electron scattering events allowed by the requirement of simultaneous conservation of energy and momentum are exchanges of the initial and final states by the participating electrons. Therefore, in wires with a small cross section, the cascadelike POP emission structure is not randomized by the interelectron collisions and an essentially new mecha-

nism of attaining the equilibrium distribution function must be formulated. In quantum dots, the usual picture for carrier thermalization by a cascade of POP emissions is invalid since a perfect matching of energy levels with separations equal to the POP energy cannot normally be achieved. Carrier equilibration on a subnanosecond scale in quantum dots, if at all possible, must be ascribed to a qualitatively different energy-loss channel. These considerations necessitate a precise microscopic description of scattering and relaxation processes in low-dimensional structures.

To exemplify the importance of the time scale of carrier thermalization for the dynamics of semiconductor laser operation, the following instance will suffice. The standard derivation of fundamental limits on the modulation speed of semiconductor lasers makes use of a phenomenological relaxation time constant, governing the exponential decay of perturbations in the carrier distribution function.^{8,9} The common practice in accounting for gain compression in semiconductor lasers is to adjust this parameter by fitting to experimental data. As a consequence, for semiconductor lasers with a bulk active layer,

a wide range of intraband relaxation times has been assumed, from 0.1 ps to several picoseconds. The nonlinear gain coefficient has also been found to determine the maximum modulation bandwidth in semiconductor lasers. Since the former is a sensitive function of the intraband relaxation time, it is particularly important to account properly for the quantum effects of carrier capture and relaxation, which are expected to dominate diffusion of carriers in the cladding layers.

In this work, we focus on the physical mechanisms responsible for carrier capture and relaxation in quantum wells, wires, and dots and endeavor to present a comprehensive numerical treatment of the problem of carrier equilibration in laser structures with quantum confinement based on semiclassical ensemble Monte Carlo simulations. These results are used to describe gain compression in quantum well, wire, and dot lasers and to derive the fundamental limits on the modulation bandwidth. The rest of the paper is organized as follows. Section II describes the theoretical formalism used in the calculation of the electronic states in quantum structures and of the scattering rates relevant to carrier relaxation

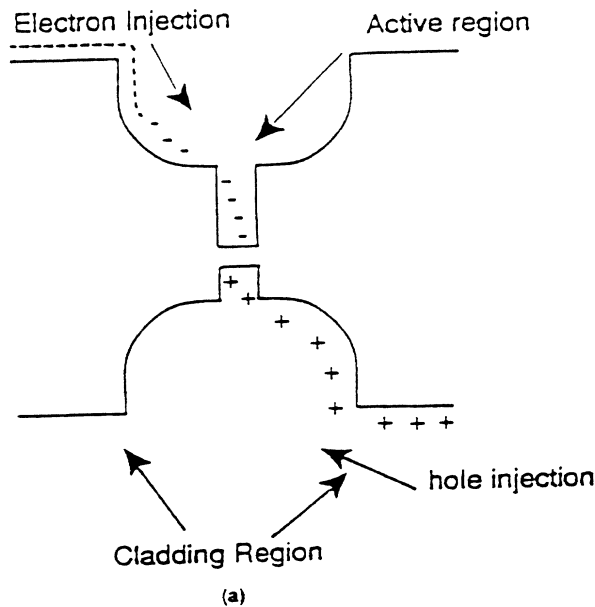
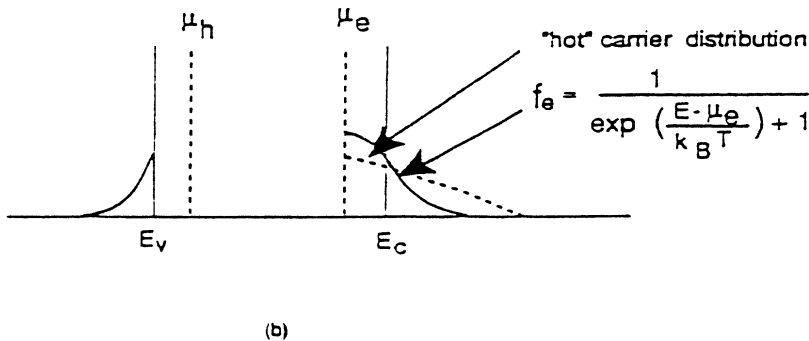


FIG. 1. (a) The cladding region and the active region of a laser. (b) The Fermi distribution for quasiequilibrium and hot carriers.



process. The structure of the Monte Carlo code is also explained. In Sec. III, results obtained from Monte Carlo simulations in quantum wells, wires, and dots are presented along with a discussion of their significance. Some conclusions based on the presented results are drawn in Sec. IV.

II. MODEL FOR CARRIER EQUILIBRATION

The treatment of the electronic states in quantum-confined structures is presented first, followed by a discussion of the theoretical model used to calculate the relevant scattering rates. The structure of the Monte Carlo code is explained next.

A. Electronic states

The quantum structures to be studied in this paper are quantum wells, wires, and dots with one, two, and three dimensions of the order of the de Broglie wavelength for electrons at room temperature, bounded in the direction of confinement by $\text{Al}_x\text{Ga}_{1-x}\text{As}$ cladding regions. The electronic states are found by a numerical solution of the effective-mass Schrödinger equation and Kohn-Luttinger Hamiltonian¹⁰ with the appropriate confining potential. The standard prescription for calculating quantum-confined states ($k_z \rightarrow -i\partial/\partial z$, etc.) is used. The length, area, and volume of the confining region for quantum wells, wires, and dots, respectively, are discretized on a uniform mesh and the electron wave function is required to vanish at the edges of the confining region by truncating the matrix expansion. The differential equation is subsequently converted into a finite-difference equation which can be readily solved by the standard iterative matrix-solving routines.

The off-diagonal terms in the Kohn-Luttinger Hamiltonian describe the deviations from the parabolic behavior of the energy bands. The breaking of the spherical rotational symmetry in quantum-well structures leads to the mixing of the states with distinct zone-center angular momentum away from the zone center and significant nonparabolicities due to anticrossing of subband levels. In quantum-wire structures, only one component of the electron wave vector may be designated a good quantum number and the resulting Hamiltonian matrix cannot be separated into heavy-hole and light-hole submatrices even at the zone center ($k_z = 0$).^{11,12}

B. Scattering rates

1. Polar optical-phonon scattering

POP scattering is caused by the interaction of carriers with local polarization fields created by lattice vibrations in polar semiconductors. The contribution of longitudinal-optical (LO) -phonon modes need only be considered since longitudinal vibrations alone are capable of setting up polarization fields. In GaAs, the electron-LO-phonon coupling via the Fröhlich interaction has been implicated as the dominant energy-loss mechanism in hot carrier thermalization. The scattering rate between any two states can be found from the Fermi golden

rule:

$$S_{i,f} = \frac{2\pi}{\hbar} \sum_{\mathbf{q}} |M_{i,f}(\mathbf{q})|^2 \delta(E_f - E_i \pm \hbar\omega), \quad (1)$$

where the Dirac delta function ensures energy conservation in the transition from the initial to the final state and the scattering is essentially instantaneous. The overlap matrix element of the perturbative part of the Hamiltonian is between the initial and final states of the electron and the phonon system. Taking into account the fact that crystal momentum is conserved in the directions with no quantum confinement, the following expressions can be written for 2D systems:

$$S_{i,f}(\mathbf{k}_{\parallel}, \mathbf{k}'_{\parallel}) = \frac{2\pi}{\hbar} \sum_{q_z} C_q \delta_{\mathbf{k}_{\parallel}, \mathbf{k}'_{\parallel} + \mathbf{q}_{\parallel}} |F_{if}(q_z)|^2 \times \delta(E_f(\mathbf{k}'_{\parallel}) - E_i(\mathbf{k}_{\parallel}) \pm \hbar\omega_q), \quad (2)$$

where the form factor is given by

$$F_{if}(q_z) = \int_{-\infty}^{\infty} dz \phi_f^*(z) \phi_i(z) e^{iq_z z}, \quad (3)$$

where the vectors with the \parallel subscript are in the x - y plane (with no quantum confinement); 1D systems,

$$S_{i,f}(\mathbf{k}_x, \mathbf{k}'_x) = \frac{2\pi}{\hbar} \sum_{q_1} C_q \delta_{\mathbf{k}_x, \mathbf{k}'_x + \mathbf{q}_x} |F_{if}(q_1)|^2 \times \delta(E_f(\mathbf{k}'_x) - E_i(\mathbf{k}_x) \pm \hbar\omega_q), \quad (4)$$

where the form factor is given by

$$F_{if}(\mathbf{q}_1) = \int d\mathbf{r}_1 \phi_f^*(\mathbf{r}_1) \phi_i(\mathbf{r}_1) e^{i\mathbf{q}_1 \cdot \mathbf{r}_1}, \quad (5)$$

where the vectors with the \perp subscript are in the y - z plane (with quantum confinement); and 0D systems,

$$S_{i,f} = \frac{2\pi}{\hbar} \sum_{\mathbf{q}} C_q |F_{if}(\mathbf{q})|^2 \delta(E_f - E_i \pm \hbar\omega_q), \quad (6)$$

where the form factor is given by

$$F_{if}(\mathbf{q}) = \int d\mathbf{r} \phi_f^*(\mathbf{r}) \phi_i(\mathbf{r}) e^{i\mathbf{q} \cdot \mathbf{r}}, \quad (7)$$

where all vectors are three dimensional.

The coupling coefficient C_q that can be found from the Fröhlich interaction Hamiltonian for the unscreened interaction is¹³

$$C_q = (n_q + \frac{1}{2} \pm \frac{1}{2}) |c_q|^2 = \frac{1}{q} \frac{(n_q + \frac{1}{2} \pm \frac{1}{2}) 2\pi e^2 \hbar\omega_{op}}{V} \left(\frac{1}{\epsilon_{\infty}} - \frac{1}{\epsilon_s} \right), \quad (8)$$

where V is the normalization volume, ϵ_{∞} and ϵ_s are the optical and static dielectric constants, respectively, $\hbar\omega_{op}$ is the (constant) LO-phonon frequency near the zone center, and n_q is the occupation number given by the Planck distribution.

In quantum wells, the expression given above must be integrated over all the final momentum space into which the electron can be scattered. Straightforward manipulations yield the following expression, which can be easily

evaluated numerically:¹⁴

$$S_{mn}^{\text{POP}} = \frac{e^2 \omega_0}{8\pi \epsilon_0} \left[\frac{1}{\epsilon_\infty} - \frac{1}{\epsilon_0} \right] \times \int \frac{H_{mn}(q)q}{q^2 + q_s^2} \delta(E(\mathbf{k}_2) - E(\mathbf{k}_1) \pm \hbar \omega_0) d\mathbf{k}_2, \quad (9)$$

where q_s is the screening constant with the dimensions of inverse length. Its introduction to account for the static screening mechanism will be justified in Sec. II C. The multisubband coupling coefficients are given by

$$H_{mn}(q) = \int \int dz_1 dz_2 \varphi_m(z_1) \varphi_n(z_1) \times \varphi_m(z_2) \varphi_n(z_2) e^{-q|z_1 - z_2|}, \quad (10)$$

Similar procedures may be followed to obtain an expression for numerical evaluation of the scattering rate in quantum wires.^{16,17} Alternatively, it is possible to model the quantum wire as a quantum dot with the length in one dimension significantly greater than the de Broglie wavelength. Then the scattering rates for quantum wires may be obtained using the expression for quantum dots in which no momentum-space integrations are necessary. The latter approach was followed in numerical calculation of the scattering rates in this paper.

The discussion above is applicable to bulk phonon modes. In semiconductor heterostructures, phonon modes are modified at the interfaces between dissimilar media. In particular, confined phonon modes may be created with the spatial structure of standing waves as well as interface modes having their extrema at the interfaces and decaying into the structure as well as hybrids between the two.¹⁵ The strength of the optical-phonon quantization in double heterostructures depends on the difference between the resonance vibration frequencies in the two materials forming the interface and the width of the heterostructure region. In separate confinement heterostructures that are currently widely used in semiconductor lasers, the confinement of the optical wave, for which a large difference in the refractive indices of the two materials, and therefore a significantly different material composition, is necessary, is realized separately from the confinement of carriers, for which a smaller step in the composition profile is normally required. Therefore, for a sufficiently small difference in the resonant frequencies, the effect of phonon quantization is likely to become important for widths less than 50 Å. However, such small features are not useful for laser active regions owing to the reduced electron-hole overlap. For various laser structures considered in this paper, we discovered that the results for the modified phonon modes do not differ significantly from those for the bulk modes. Therefore, in the following, in order to simplify our presentation, we ignore the modifications of phonon modes caused by the heterostructures and quote the results for bulk phonons alone.

In 1D and 0D electronic systems, the density of states exhibits singularities. To treat this problem, it is neces-

sary to calculate the scattering rates in a self-consistent fashion, i.e., including the energy-level broadening given by the imaginary part of the electron self-energy. The broadening linewidth may be found iteratively once the line shape is known. In our calculations a Gaussian line shape (a good approximation for the sum of the contributions of the variety of different mechanisms responsible for the broadening) was used in place of the δ function:

$$\delta(E_f - E_i \pm \hbar \omega_{\text{LO}}) \rightarrow \frac{1}{\sqrt{1.44\pi\sigma}} \exp\left[-\frac{(E_f - E_i \pm \hbar \omega_{\text{LO}})^2}{1.44\sigma^2}\right], \quad (11)$$

where the linewidth σ is proportional to the scattering rate. The iterative calculation proceeds until the scattering rate sufficiently consistent with the assumed linewidth is found numerically. This procedure may be regarded as accounting for renormalization of the electron and phonon spectra by mutual interaction, in which initially sharp levels are broadened as a consequence of the potential (virtual) interaction. The energy is required to be conserved only to the precision of the linewidth given by the scattering rate.

2. Acoustic-phonon scattering

Acoustic-phonon scattering is physically attributed to the strain created by the acoustic branch of quantized lattice vibrations and is usually treated using the deformation-potential theory formalism.¹⁸ The scattering rate is easily obtained in the long-wavelength limit in which the matrix element is directly proportional to the phonon wave vector. In bulk material, the phonon wave vectors involved in transitions are very close to the zone center, and the exchange of energy in an acoustic-phonon scattering event is sufficiently small to be neglected in Monte Carlo simulations. The elastic approximation becomes progressively poorer as one proceeds to structures with greater quantum confinement.^{19,20} The inelasticity is caused by the uncertainty in the momentum conservation introduced by the lack of translational symmetry in the directions with quantum confinement. Assuming that the electron wave function is confined while phonon modes are not appreciably different from the bulk ones, it is possible to recalculate the acoustic-phonon scattering rates using the exact form of the matrix element. The expressions (1)–(7) can be used to find the scattering rate with the following coupling coefficient:

$$C_q = \frac{(n_q + \frac{1}{2} \pm \frac{1}{2}) D_A^2 q^2 \hbar}{2V\rho\omega_q}, \quad (12)$$

where D_A is the (constant) acoustic deformation potential near the zone center and ρ is the material mass density. The linear dispersion relation may be used to relate the phonon wave vector and frequency

$$\omega_q = \bar{v}_s q, \quad (13)$$

where \bar{v}_s is the velocity of the acoustic-phonon mode averaged over direction. The scattering rate may now be evaluated numerically. If the elastic approximation is made, the scattering rate in 2D becomes simply

$$S_{mn} = \frac{m^* k_B T D_A^2}{\hbar^3 \rho v_s^2} \int \varphi_m^2(z) \varphi_n^2(z) dz. \quad (14)$$

3. Electron-electron scattering

In the Born approximation, electron-electron interaction leads to an energy-conserving scattering mechanism. The strength of electron-electron scattering is proportional to the carrier density. The treatment of electron-electron scattering in bulk regions has been discussed.^{21,22} The matrix element is given by

$$M_{i,m,j,n}^{ee}(\mathbf{k}_1, \mathbf{k}'_1, \mathbf{k}_2, \mathbf{k}'_2) = \frac{e^2}{V \epsilon_0} \int d\mathbf{r} \int d\mathbf{r}' e^{-q_s |\mathbf{r}-\mathbf{r}'|} \frac{e^{-i(\mathbf{k}'_1 \cdot \mathbf{r} + \mathbf{k}'_2 \cdot \mathbf{r}')} e^{i(\mathbf{k}_1 \cdot \mathbf{r} + \mathbf{k}_2 \cdot \mathbf{r}')}}{|\mathbf{r}-\mathbf{r}'|} = \frac{4\pi e^2}{V \epsilon_0} \frac{\delta_{\mathbf{k}_1 + \mathbf{k}_2, \mathbf{k}'_1 + \mathbf{k}'_2}}{|\mathbf{k}_1 - \mathbf{k}_2|^2 + q_s^2}, \quad (15)$$

where ϵ_0 is the static dielectric constant of the material and q_s is the inverse screening length, assumed to be independent of the wave vector. The total scattering rate out of an electronic state \mathbf{k}_2 can be found from

$$S_{e-e}(\mathbf{k}_2) = \frac{nm^* e^4}{4\pi \hbar^3 \epsilon_0 q_s^2 N} \sum_{\text{all } k'_s} \frac{|\mathbf{k}_1 - \mathbf{k}_2|}{q_s^2 + |\mathbf{k}_1 - \mathbf{k}_2|^2}, \quad (16)$$

where N is the number of simulated electrons, n is the electron concentration, and the sum is over all electron states. A rejection method can be used, in which the maximum value of the term dependent on the wave-vector difference is assumed in order to find the maximum scattering rate

$$S_{e-e,3D,\max} = \frac{m^* e^4 n}{8\pi \hbar^3 \epsilon_0^2 q_s^3}. \quad (17)$$

A rejection method is also used to account for the occupation of the final states available to the electron.²³ The details of the implementation of the Monte Carlo simulation are described in Sec. II D.

In 2D the matrix element involves an integration over the envelope function of the confined states²⁴

$$M_{i,m,j,n}^{ee}(\mathbf{k}_{1,\parallel}, \mathbf{k}'_{1,\parallel}, \mathbf{k}_{2,\parallel}, \mathbf{k}'_{2,\parallel}) = \frac{e^2}{V \epsilon_0} \int dz \int dz' \int d\mathbf{r}_{\parallel} \int d\mathbf{r}'_{\parallel} e^{-q_s [|\mathbf{r}_{\parallel} - \mathbf{r}'_{\parallel}|^2 + (z - z')^2]^{1/2}} \frac{e^{-i(\mathbf{k}'_{1,\parallel} \cdot \mathbf{r}_{\parallel} + \mathbf{k}'_{2,\parallel} \cdot \mathbf{r}'_{\parallel})} e^{i(\mathbf{k}_{1,\parallel} \cdot \mathbf{r}_{\parallel} + \mathbf{k}_{2,\parallel} \cdot \mathbf{r}'_{\parallel})}}{[|\mathbf{r}_{\parallel} - \mathbf{r}'_{\parallel}|^2 + (z - z')^2]^{1/2}} \varphi_i(z) \varphi_j(z') \varphi_m^*(z) \varphi_n^*(z'). \quad (18)$$

Evaluation of the square of the matrix element yields

$$|M_{i,m,j,n}^{ee}(\mathbf{k}_{1,\parallel}, \mathbf{k}'_{1,\parallel}, \mathbf{k}_{2,\parallel}, \mathbf{k}'_{2,\parallel})|^2 = \frac{4\pi^2 e^4 \delta(\mathbf{k}'_{1,\parallel} + \mathbf{k}'_{2,\parallel} - \mathbf{k}_{1,\parallel} - \mathbf{k}_{2,\parallel})}{A^2 \epsilon_0^2 (q + q_s)^2} |F_{ijmn}(q)|^2, \quad (19)$$

where A is the normalization area, and the multisubband coupling coefficients

$$F_{ijmn} = \int_{-\infty}^{\infty} dz \int_{-\infty}^{\infty} dz' \varphi_i(z) \varphi_j(z') \varphi_m^*(z) \varphi_n^*(z') e^{-q|z-z'|} \quad (20)$$

are similar to those needed to evaluate the polar optical-phonon scattering rate. The total scattering rate into all momentum-space states can be determined by integration of the square of the matrix element above. Using the requirements of conservation of energy and momentum, the integrations can be reduced to a single one:

$$S_{e-e,im}(\mathbf{k}_2) = \frac{4\pi e^4 m^*}{\hbar^3 A \epsilon_0^2} \sum_{\mathbf{k}_2, j, n} f_j(\mathbf{k}_2) \int_0^{2\pi} d\theta \frac{|F_{ijmn}(q)|^2}{(q + q_s)^2}, \quad (21)$$

where θ represents the angle between the relative wave vectors $\mathbf{g} = \mathbf{k}_2 - \mathbf{k}_1$ and $\mathbf{g}' = \mathbf{k}'_2 - \mathbf{k}'_1$, whose magnitude is equal in accordance with the requirement of conservation of energy. It is clear that the electron-electron scattering rate is dependent on the distribution function, which is the quantity we set out to determine in the Monte Carlo simulation. Although this does not represent a problem *per se*, the evaluation of the distribution function in the Monte Carlo simulation proceeds in very small time steps and the simulation time may be considerably increased owing to the necessity of recalculating the scattering rates for each time interval. It turns out that a rejection technique yields much more efficient results. The only rate that needs to be evaluated is the maximum scattering rate which remains constant during the simulation. The result for the maximum intrasubband scattering rate is²⁴

$$S_{e-e,\max,ii} = \frac{4\pi^2 e^4 m^* N_s}{\hbar^3 \epsilon_0^2 q_0^2}, \quad (22)$$

where N_s is the electron sheet density in the quantum well. The maximum intersubband scattering rate must be multiplied by the square of the maximum value of the multisubband coupling coefficient and the total number

of subbands. A rejection method is also used to account for the finite occupation probability of the final states.

One-dimensional systems are distinguished by the fact that intrasubband electron-electron scattering cannot affect the shape of the distribution function because the only allowed scattering process merely exchanges the en-

ergies and momenta of the electrons. Thus, in quantum wires with a small cross section, in which only one or two subbands lie below the conduction-band discontinuity, randomization of the distribution function by electron-electron scattering does not occur or occurs very slowly.

In 1D, the matrix element takes the form²⁵

$$M_{i,m,j,n}^{ee}(k_1, k'_1, k_2, k'_2) = \frac{e^2}{V\epsilon_0} \int d\mathbf{r}_1 \int d\mathbf{r}'_1 \int dx \int dx' e^{-q_s[(x-x')^2 + |\mathbf{r}_1 - \mathbf{r}'_1|^2]^{1/2}} \frac{e^{-i(k'_1 x + k'_2 x')} e^{i(k_1 x + k_2 x')}}{[(x-x')^2 + |\mathbf{r}_1 - \mathbf{r}'_1|^2]^{1/2}} \varphi_i(\mathbf{r}_1) \varphi_j(\mathbf{r}'_1) \varphi_m^*(\mathbf{r}_1) \varphi_n^*(\mathbf{r}'_1). \quad (23)$$

The integrations over x and x' may be carried out analytically to yield

$$M_{i,m,j,n}^{ee}(k_1, k'_1, k_2, k'_2) = \frac{e^2}{2\pi\epsilon_0 L} \int d\mathbf{r}_1 \int d\mathbf{r}'_1 \varphi_i(\mathbf{r}_1) \varphi_j(\mathbf{r}'_1) \varphi_m^*(\mathbf{r}_1) \varphi_n^*(\mathbf{r}'_1) \times \delta(k_1 + k_2 - k'_1 - k'_2) \times K_0(|q_x ||\mathbf{r}_1 - \mathbf{r}'_1|), \quad (24)$$

where K_0 is the zeroth-order modified Bessel function, q_x is the wave vector exchanged in the x direction, $k'_1 - k_1$, and L is the length of the wire. The scattering rate may be evaluated by a subsequent integration over the final momentum space. By including the subband-edge energies into the energy-conservation equation and solving the energy- and momentum-conservation equations for the possible values of the exchanged momentum in the x direction, a quadratic equation results with the implication that only two final scattering states are available. If the two carriers remain in their respective subbands, such scattering is equivalent that in a truly one-dimensional system and the scattering process is irrelevant since the particles are indistinguishable. However, significant energy exchanges between subbands are possible if carriers end up in subbands different from the original ones. In this paper, we treat electron-electron scattering in quantum wires by extending the case of quantum dots treated below to a quantum dot with the length in one dimension greatly exceeding the de Broglie wavelength. By comparing the results with the one-dimensional treatment, we find that they converge for a sufficiently large value of the length of the quantum wire.

Electron-electron scattering in quantum dots is straightforward to model owing to the complete confinement of the electronic states. The scattering rate can be readily found from the Fermi golden rule using the following form of the matrix element:

$$M_{i,m,j,n}^{ee} = \frac{e^2}{V\epsilon} \int d\mathbf{r} \int d\mathbf{r}' e^{-q_s |\mathbf{r} - \mathbf{r}'|} \times \frac{\varphi_i(\mathbf{r}) \varphi_j(\mathbf{r}') \varphi_m^*(\mathbf{r}) \varphi_n^*(\mathbf{r}')}{|\mathbf{r} - \mathbf{r}'|}. \quad (25)$$

The scattering rates in quantum wires and dots must be evaluated self-consistently in the manner described above for phonon scattering.²⁶

4. Electron-hole scattering

The formalism for electron-hole scattering²⁷ is essentially identical to that for electron-electron scattering except that a sum over all valence-band states obtained by solving the Kohn-Luttinger Hamiltonian is necessary. In order to simplify the problem of electron-hole scattering in structures with quantum confinement we avoid the necessity of dealing with mixed states of angular momentum and instead make the parabolic-band approximation in which the off-diagonal elements of the Kohn-Luttinger Hamiltonian are set to zero. This is clearly unacceptable in problems where the mixing is critical to the correct description of the problem, for example, in accounting for the polarization dependence of optical transitions in structures with quantum confinement. However, in our attempt to describe electron-hole scattering, this approximation is desirable to avoid tedious calculations with long computation times. Therefore, it is made in our treatment of electron-hole scattering.

A full Monte Carlo simulation for two types of carriers is extraordinarily time consuming and difficult computationally. However, using the approximation that the relaxation processes in the valence band are considerably faster than those in the conduction band (so that the hole distribution is always maintained in thermal equilibrium with the lattice), the problem is considerably simplified since electron-hole scattering affects only carriers in the conduction band. In fact, it is simpler than the problem of electron-electron scattering since the hole distribution is known *a priori*. The approximation made depends on the assumptions that the phonon-hole scattering rates in a quantum wire are much greater than phonon-electron scattering rates and that complete thermalization of the hole distribution takes place essentially instantaneously. While the latter assumption is somewhat questionable given the difficulties in thermalization experienced by the electron gas in quantum wires and quantum dots, in our view, it is the best way to obtain at least an approximate quantitative idea of the magnitude of the electron-hole scattering rates.

C. Screening effects

Screening in semiconductors may have a dramatic effect on the scattering rate provided the carrier concentration is sufficiently high to modify the form of the potential with which carriers are interacting. The problem of self-consistent screening in the random-phase approximation is difficult computationally, requiring an inversion of the dielectric matrix of the multisubband system.²⁸ This procedure is not a practical one in standard Monte Carlo simulations. Instead the static, long wavelength limit is taken, which yields results identical to the well-known Thomas-Fermi approximation. The effects of screening can be characterized by a single wave-vector-independent quantity. The dielectric function becomes simply

$$\epsilon(q) = 1 + \frac{\lambda^2}{q^2}, \quad (26)$$

where λ is the inverse Debye screening length, given by

$$\lambda^2 = \frac{e^2 n}{\epsilon k_B T}, \quad (27)$$

where n is the carrier concentration. Although this expression is valid only for nondegenerate carrier statistics, we use it throughout our calculations in this work in order to simplify our approach to the screening problem. Since the effects of screening on the electron-phonon and carrier-carrier interactions in multiple-subband quantum wires are still unclear at present, it is reasonable to resort to such an approximation. The presence of a large concentration of holes in the active region leads similarly to electrostatic screening. The simplest way of accounting for the effect of hole screening is to add the electrons and hole concentrations and substitute the result in the expression for the screening length, Eq. (27). In this paper, we are primarily concerned with the effect of order-of-magnitude changes in the carrier density on electron relaxation. Therefore, the above-mentioned distinction is of secondary importance.

While acoustic-phonon scattering is presumed to be unaffected by the screening mechanisms, the polar optical-phonon scattering rate has to be modified to account for its effects. The formulas given above incorporate the effect of screening in terms of the phenomenological screening wave vector q_s , which is now identified with λ .

D. Monte Carlo simulation

In our Monte Carlo simulation, carrier transport in the 3D and lower-dimensional regions is modeled separately. In constructing the Monte Carlo approach to carrier equilibration in lower-dimensional regions, a small region of the cladding region as well as the confined region are taken into account in computing the band structure.²⁹ In particular, the 3D-2D simulation is done for a graded-index cladding structure, in which a thin layer of the neighboring barrier may also experience rather strong confinement effects. The transitions between the 3D and 2D regions are based on the assumption that if a 2D Monte Carlo calculation for the graded region is carried

out including all subbands, then in principle the same result can be obtained from the corresponding 3D Monte Carlo calculation. In practice, it is only necessary to consider up to five subbands.^{30,31} The 3D \rightarrow 2D and 2D \leftarrow 3D transitions are modeled as phonon-assisted processes. A transition energy level E_{tr} is introduced to facilitate the 3D-2D transition. The 3D \rightarrow 2D transition is carried out if, upon the termination of a 3D free flight, the total carrier energy after a phonon emission scattering process is expected to fall below E_{tr} . A final 2D state is chosen from the nearest subband considering energy and momentum conservation. We perform the reverse 2D \rightarrow 3D transition when the total energy of a well carrier is expected to exceed E_{tr} after a phonon absorption scattering process. To conserve the in-plane energy and momentum, the in-plane wave vector is unchanged. The z component of the wave vector is then obtained by taking into account energy conservation; its z orientation is randomly selected. In our study, we set E_{tr} equal to one $k_B T$ (26 meV) above the subband minimum of the highest (fifth) state being considered. This setting is confirmed with a series of simulation runs. Essentially no change is observed if E_{tr} is increased somewhat, showing that including five subband levels is quite adequate.

A similar procedure is followed for 3D-1D and 3D-0D simulations. The graded-index cladding regions are not considered, however, in order to simplify the computational procedure. Moreover, the state of the art in defining quantum wires and quantum dots has not reached the stage in which fabrication of practical semiconductor lasers is possible; therefore, the need for greater precision in our simulations is less urgent. The Monte Carlo code simulates the evolution of the energy distribution of an ensemble of electrons injected in a thermal distribution above the top of the potential barrier created by the conduction-band discontinuity. The energy spectrum is divided into a large number of intervals of equal and small extent. The standard Monte Carlo procedure with the introduction of self-scattering events is followed allowing for the needed number of degrees of freedom of the particles. The results are averaged over a large number (5000–10 000) of electrons in order to suppress stochastic fluctuations in the results.

The time of the simulations is divided into very short intervals of the order of 1 fs. Thus it is ensured to a high degree of precision that no more than one scattering event can occur in each time interval. Carrier-carrier scattering and finite occupancy of the final states necessitate the introduction of additional self-scattering mechanisms. This allows computing the scattering rate only once in the process of the simulation, which reduces the required computing time considerably. The distributions of carriers in time and energy are tabulated, and the results are found by averaging.

E. Linear and nonlinear gain formalism

Although the Monte Carlo approach described above allows immediate determination of such quantities as the average capture and thermalization times and the fraction of the carriers escaping from the well region, addi-

tional calculations are necessary to ascertain the effect of a finite thermalization time on the characteristics of semiconductor lasers. Since the effect of the thermalization time is to introduce a correction to the gain spectrum at high photon densities present in the laser cavities (corresponding to high rates of stimulated emission), it is necessary first to compute the linear gain of each simulated structure neglecting excitonic effects. The optical gain can be calculated using the Fermi golden rule and a knowledge of the conduction- and valence-band structures.³² The latter part of the problem has been discussed above. The expressions for the material gain are (in Gaussian units), in 2D, 1D, and 0D, respectively,

$$g(\hbar\omega) = \frac{4\pi^2 e^2 \hbar}{n_a c m_0^2 \hbar \omega} \frac{1}{W} \frac{2}{(2\pi)^2} \times \int d\mathbf{k} \sum_{n,m} |\hat{\epsilon} \cdot \vec{P}_{nm}(\mathbf{k})|^2 \delta(E_n^c(\mathbf{k}) - E_m^v(\mathbf{k}) - \hbar\omega) \times [f^c(E_n^c(\mathbf{k})) - f^v(E_m^v(\mathbf{k}))], \quad (28)$$

$$g(\hbar\omega) = \frac{4\pi^2 e^2 \hbar}{n_a c m_0^2 \hbar \omega} \frac{1}{A} \frac{2}{2\pi} \times \int dk \sum_{n,m} |\hat{\epsilon} \cdot \vec{P}_{nm}(k)|^2 \delta(E_n^c(k) - E_m^v(k) - \hbar\omega) \times [f^c(E_n^c(k)) - f^v(E_m^v(k))], \quad (29)$$

$$g(\hbar\omega) = \frac{4\pi^2 e^2 \hbar}{n_a c m_0^2 \hbar \omega} \frac{2}{V} \sum_{n,m} |\hat{\epsilon} \cdot \vec{P}_{nm}|^2 \delta(E_n^c - E_m^v - \hbar\omega) \times [f^c(E_n^c) - f^v(E_m^v)], \quad (30)$$

where W , A , and V are the width, area, and volume of the confined region, respectively, $\hat{\epsilon}$ is the unit vector in the direction of light polarization, \vec{P}_{nm} is the momentum matrix element between the conduction- and valence-band states, f^c and f^v are the conduction and valence-band functions assumed to be described by quasi-Fermi statistics for the purposes of obtaining the linear gain, and the rest of the symbols have their usual meaning. The carrier distribution is presumed to be in thermal equilibrium with the lattice. The actual calculation proceeds by adjusting the quasi-Fermi levels until the hole density is equal to the desired electron density.

In a practical semiconductor laser, the assumption of Fermi-Dirac distributions in the conduction band breaks down far above threshold. The distribution function achieves a steady-state profile determined by the interplay of intense stimulated emission near the lasing wavelength and carrier injection at the top of the potential barrier.³³ The lasing characteristics in this case must in principle be evaluated via a self-consistent calculation of the intensity of the electromagnetic field in the cavity expressed in terms of the photon density, the carrier density, and the distribution determining the pattern of interaction with the electromagnetic field.³⁴ In practice such a calculation is extremely lengthy and tedious when

carried out numerically. A simpler model used in theoretical calculations is to introduce a nonlinear gain term into the rate equations.^{35,36} The optical gain thus becomes a function of the photon density, and phenomenological self-consistency is achieved. Our objective, therefore, is to determine the dependence of the optical gain on carrier density by finding the exact shape of the distribution function under intense stimulated emission.

In the case of the quantum-well laser, we find it convenient to carry out the calculation in a nonlasing mode, i.e., in an equivalent optical amplifier. This eliminates the necessity of maintaining the gain of the mode at a fixed value equal to the cavity losses, as the correct description of the lasing mode would require. The nonlinear gain term in semiconductor lasers has been introduced in several ways. For a product of the photon density and the nonlinear gain coefficient much less than unity, by using an expansion in terms of this product, all possible expressions are adequately reproduced by neglecting all terms higher than the first power. The optical gain thus becomes $g(n, S) = g(n)[1 - \epsilon S]$. It is plain that the following convenient definition of the nonlinear gain coefficient may be adopted:

$$\epsilon = - \left. \frac{\Delta g}{\Delta S} \frac{1}{g_0} \right|_{S=0}, \quad (31)$$

where S is the photon density and g_0 is the extrapolated gain at $S=0$. Two steady-state results of the Monte Carlo simulation, one with $S=0$ (peak optical gain g_1) and the other with a finite S_2 (peak optical gain g_2) are used. The effect of stimulated emission is incorporated into the Monte Carlo simulation by extracting a certain number of carriers, consistent with the necessary rate of stimulated emission, and allowing the distribution function to converge to a steady state. The gain compression parameter is then approximately

$$\epsilon = - \frac{g_2 - g_1}{S_2} \frac{1}{g_1}. \quad (32)$$

The photon density S_2 can be found easily from the rate equation for the carrier density.

An alternative theoretical formalism³⁷ for determining the steady-state form of the distribution function has been also developed and applied to the quantum-wire laser problem. It relies on a direct solution of the Boltzmann equation for the laser problem rather than on the full Monte Carlo simulation that may often become excessively cumbersome. This approach is particularly well suited to the quantum-wire problem in which polar optical-phonon scattering represents the major scattering mechanism by virtue of its relative strength and the rest of the scattering mechanisms may be modeled as perturbations contributing a finite lifetime of the energy levels expressed as energy-level broadening. The evolution of the system in time is described by the Boltzmann equation for a spatially homogeneous system with no applied fields:

$$\begin{aligned} \frac{\partial f(E)}{\partial t} = & f(E + \hbar\omega)[1 - f(E)]W_{\text{ems}}(E + \hbar\omega, E) \\ & + f(E - \hbar\omega)[1 - f(E)]W_{\text{abs}}(E - \hbar\omega, E) \\ & - f(E)[1 - f(E + \hbar\omega)]W_{\text{abs}}(E, E + \hbar\omega) \\ & - f(E)[1 - f(E - \hbar\omega)]W_{\text{ems}}(E, E - \hbar\omega), \quad (33) \end{aligned}$$

where W_{ems} and W_{abs} represent the integrated scattering rates for emission and absorption of phonons, respectively, over all \mathbf{k} states at corresponding energies. The time derivative must be set to zero in order to solve for the steady-state distribution function. It is straightforward to verify that any function satisfying the condition of detailed balance

$$n_q[1 - f(E + \hbar\omega)]f(E) = (n_q + 1)f(E + \hbar\omega)[1 - f(E)], \quad (34)$$

where n_q is the phonon occupation number, is the solution of the above equation. The effects of stimulated emission at the lasing wavelength and carrier injection at the edge of the potential barrier are now taken into account by introducing the source and sink terms obtained from the rate equation for the carrier density. The energy spectrum of interest is then subdivided into small intervals and the Boltzmann equation is converted into a set of coupled nonlinear equations. The equations are greatly simplified if only POP scattering is included because only points separated by multiples of the optical-phonon energy are coupled. The rest of the scattering rates calculated from the formalism presented above are then treated as contributing a lifetime broadening with the linewidth proportional to the total scattering rate in each interval.

A direct numerical solution of the resulting set of equation is cumbersome for a fine mesh on the energy spectrum. Instead the problem can be solved by an iterative Monte Carlo approach. A Fermi-Dirac distribution function is taken initially for electrons with the implicit assumption that the final steady-state distribution function does not deviate strongly from the canonical form. Next the distribution function is substituted into Eq. (33) with the source and sink terms describing the effects of an injection current density J into the active region and stimulated emission at the lasing energy for a photon density S . Random perturbations of the distribution function with the maximum amplitude of 5% are made by a Monte Carlo-style technique. If the time derivative of the electron distribution function as expressed by Eq. (33) with the source and sink terms is reduced by the perturbations, the randomly generated change in the distribution function is accepted; otherwise, it is rejected. Provided the error in the time derivative is within the round-off tolerance (typically $\approx 0.1\%$ of the original error), the simulation is terminated, yielding the steady-state distribution function in the presence of intense stimulated emission.

III. RESULTS

In this section we will present results on carrier thermalization in quantum-well, quantum-wire, and

quantum-dot structures. We start with the quantum-well structure, which is the most widely used structure for low threshold lasers.

A. Carrier thermalization in quantum wells

In an ideal quantum-well structure, the well should be narrow enough ($< 100 \text{ \AA}$) so that electrons are essentially in the ground state of the conduction band. We examine a typical quantum well structure shown in Fig. 2, which is a 50- \AA GaAs/ $\text{Al}_{0.3}\text{Ga}_{0.7}\text{As}$ quantum well with a linear graded-index (L-GRIN) cladding region. The electrons are injected at the top of the “funnel” where they have energies of $\approx 0.3\text{--}0.4 \text{ eV}$ above the ground-state energy of the quantum well. In Fig. 2(a) we show the first five envelope functions for the structure and in Fig. 2(b) we show the corresponding energy levels.

In the quantum-well structure, the dominant scattering mechanism is polar optical-photon emission. The calculated values of the intersubband scattering rates are shown in Fig. 3. These rates provide insight into why the thermalization times increase in quantum-confined structures. Notice that intrasubband rates are $\approx 10^{13} \text{ s}^{-1}$, which is similar to the bulk or 3D polar optical emission rates. This rate would suggest that an energy loss of $\approx 10\hbar\omega_{\text{op}}$ ($= 0.36 \text{ eV}$ in GaAs) would take only $\approx 1 \text{ ps}$. This is indeed the case for 3D energy loss. However, one notices from Fig. 3 that intersubband rates are dramatically suppressed. For example, the scattering of an electron in the second subband to the first subband takes $< 10^{12} \text{ s}^{-1}$, and from the third subband to the first sub-

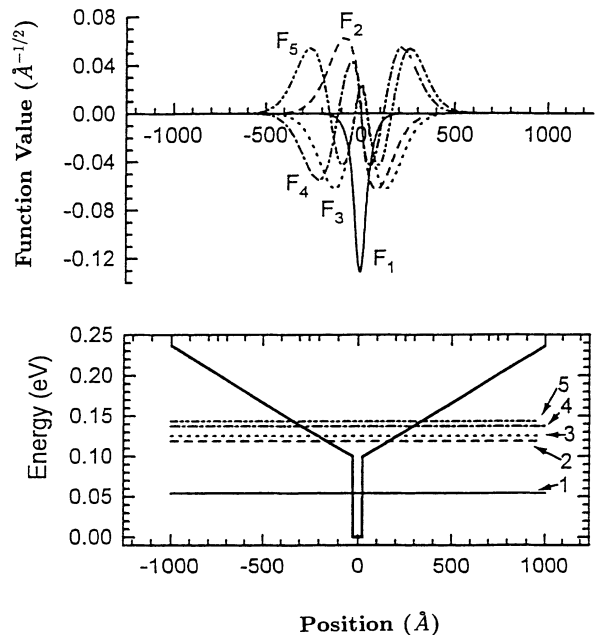


FIG. 2. First five eigenvalues and envelope parts of the eigenfunctions calculated for the 50 \AA $\text{Al}_{0.3}\text{Ga}_{0.7}\text{As}$ GRIN quantum well.

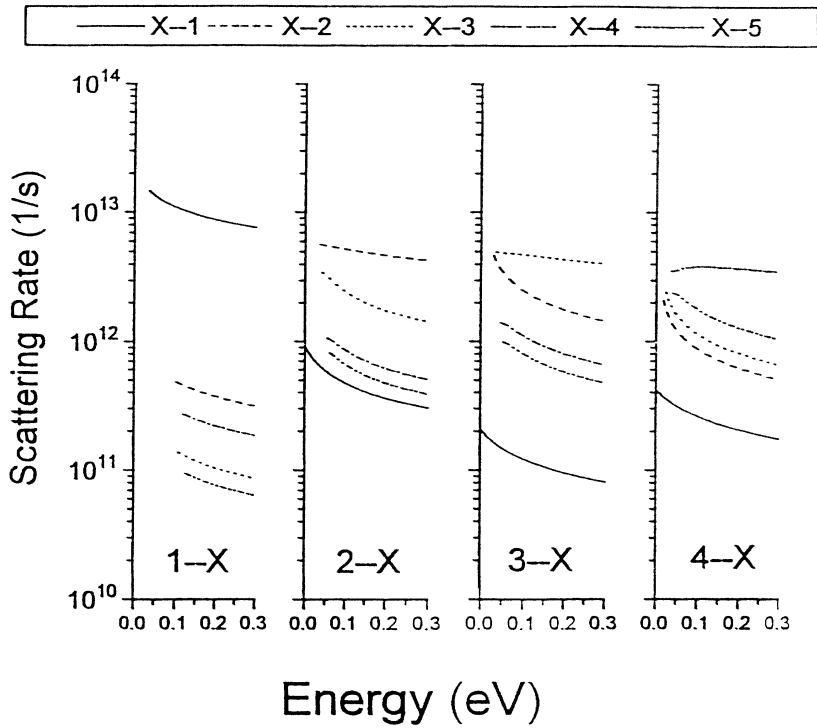


FIG. 3. Intersubband scattering rates in the 50-Å $\text{Al}_{0.3}\text{Ga}_{0.7}\text{As}$ GRINSCH quantum well. The energy abscissa is referenced from the subband minimum of the ground state.

band it is $< 2 \times 10^{11} \text{ s}^{-1}$. Since electrons must go from the higher subbands to the lower subbands during thermalization, a bottleneck is created.

In Fig. 4, we show the path a typical electron takes as it loses its excess energy in the laser structure. The paths in the energy domain and in the spatial domain are

shown. It is obvious that the carrier does not simply take the most direct path to the well, but instead spends a substantial amount of time “bouncing” around before its eventual capture by the quantum well occurs. It is also clear that the bulk of the time in the thermalization process is spent in the 2D region primarily due to suppres-

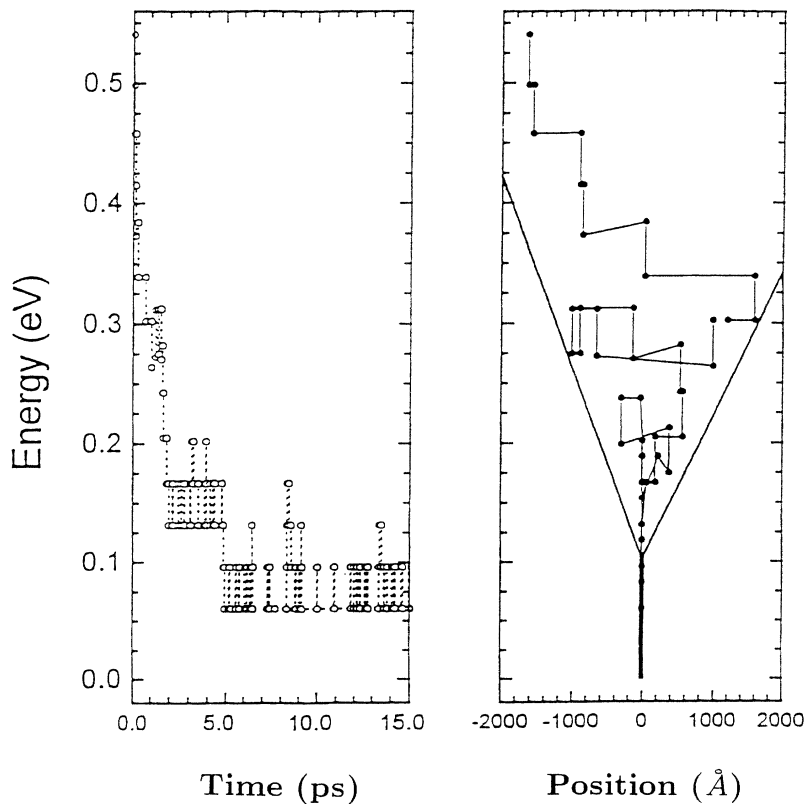


FIG. 4. Flight dynamics of an arbitrary carrier in the ensemble for the 50-Å $\text{Al}_{0.3}\text{Ga}_{0.7}\text{As}$ GRINSCH quantum well with $E_i = 15 \text{ meV}$ and an applied electric field of 2 kV/cm.

sion of intersubband scattering rates. To obtain a reasonably correct picture of the relaxation process, a statistical average over a large number of carriers ($\approx 10\,000$) must be performed. The result for the time development of the ensemble energy distribution under the low injection condition (10^{16} cm^{-3}) for the 50-Å well linearly graded-index separate confinement heterostructure (L-GRINSCH) is shown in Fig. 5. The distribution of carriers in the structure for the same simulation is shown in Fig. 6. The fraction of carriers in the "3D-GRIN" region decreases from a maximum of 100% upon injection to a low of 3% after about 15 ps, while the well-state (first subband) occupancy increases from zero to its maximum in the same period. We further note that the occupancies of the various subbands do indeed correctly portray the transport of the carriers through the subbands.

An interesting difference between the L- and P- (parabolically) GRINSCH structures lies in the carrier capture time. As shown in Fig. 7 (curves 5 and 6), the relaxation process in the L-GRINSCH structures is significantly faster than in the P-GRINSCH structures. We have also obtained good agreement between our simulation and published experiments,³⁸ by comparing the calculated carrier capture time constants of 6.7 and 8.8 ps (obtained from exponential curve fitting) and the experimental time constants of 8.2 and 10 ps, for L-GRINSCH and P-GRINSCH structures, respectively, with a well width of 50 Å.

An understanding of how the capture time changes (if at all) with the well width and the carrier injection density is crucial for optimization of the laser structure for high-speed operation. While some experiments report no

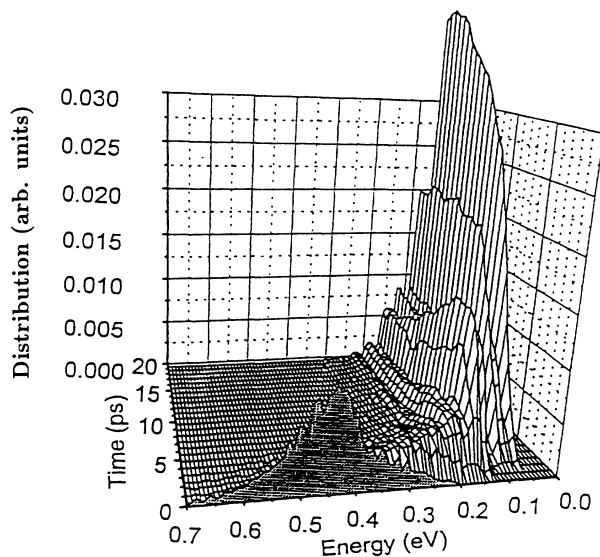


FIG. 5. Time evolution of the energy distribution for an ensemble of 10 000 relaxing carriers, injected from the edge of the confinement layer with a kinetic energy of 15 meV at time 0 ps. The simulation is performed for the structure of Fig. 3 with an applied electric field of 2 kV/cm.

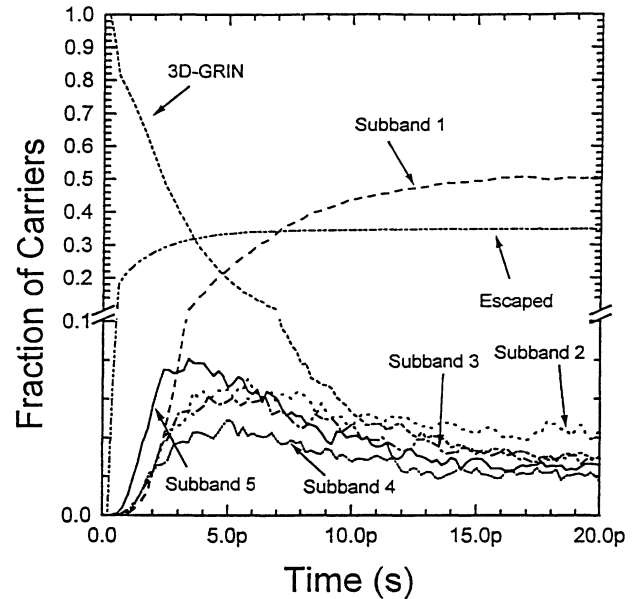


FIG. 6. The distribution of carriers in the structure of Fig. 3 as a function of time.

well-width dependence, others observe either an increasing or a decreasing trend. From Fig. 7 (curves 3–5), we see that the carrier capture time increases with the density of carrier injection. Also the capture time exhibits a nonmonotonical trend with the well width at low injections. Oscillatory behavior has been predicted by Brum *et al.*³⁹ At higher injections, monotonical trends appear.

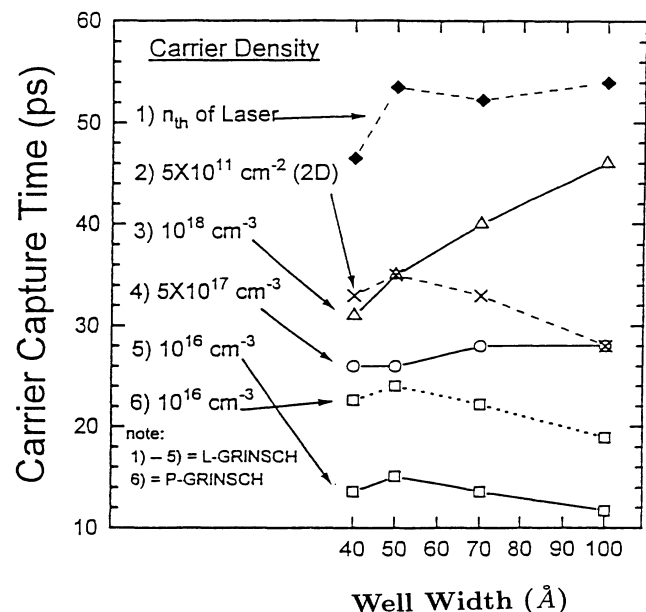


FIG. 7. Calculated carrier capture time as a function of well width and injection density. The capture time is defined as the time needed for the well-state occupancy to reach 95% of the equilibrium value.

We can observe from Fig. 7 decreasing, flat, or increasing variation of capture times with the well width, depending on the injection conditions. Longer capture times in wider well structures under high injection and no significant capture time dependence on the well width under moderate carrier injections have also been reported experimentally by Weiss *et al.*⁴⁰ On the other hand, the experiments with photoluminescence and photoexcitation measurements reported no dependences of the carrier capture time on the well width.⁴¹ Since moderate carrier injections are to be expected in these experiments, they also appear to agree with our simulation results.

We shall now examine the well-width dependence under lasing conditions, where the threshold carrier density n_{th} varies with the well size. Table I enumerates the calculated n_{th} for the L-GRINSCH lasers having typical laser parameters.³² Curve 1 in Fig. 7 shows the calculated capture times at threshold densities. We observe that the carrier capture times under lasing conditions are more or less independent of the well width. This behavior may be attributed to two opposing factors—changes in the 2D and 3D carrier densities.

For a particular 3D injection density, the 2D carrier density in the quantum well increases with the well width. Since carrier screening in the well varies with the 2D carrier density, an increase in the carrier capture time with the increasing well width may be expected. This behavior is confirmed by comparing curve 2 (constant 2D density) and curve 3 (constant 3D density) in Fig. 7. Under lasing conditions, the 2D n_{th} increases with the well size (by 20% from the 40- to the 100-Å well). Hence the capture time should be proportionally longer in the wider well lasers. On the other hand, from Table I, we note that the increases in the 2D n_{th} are accompanied by decreases in the 3D n_{th} (to 50% of its value when the well width is increased from 40 to 100 Å). Faster capture times are expected from a lower 3D carrier density. If we were to consider only the effects of 3D carrier screening and assume a square-root relationship, a 30% reduction in the capture time may be expected. However, the actual effect is much smaller since the average carrier dwell time in the 3D graded-index region is a minor portion of the overall capture time. The trend in curve 1 indicates that this effect is less than 10%.

The effect of a finite carrier capture time on the optical gain spectra of a quantum-well material can be evaluated by a combination of a macroscopic calculation of the gain spectra and the electron-photon rate equations and a microscopic simulation of a carrier dynamics as described above. The results for initial and final optical spectra when a finite photon density is introduced into the cavity are shown in Fig. 8. The gain compression coefficient

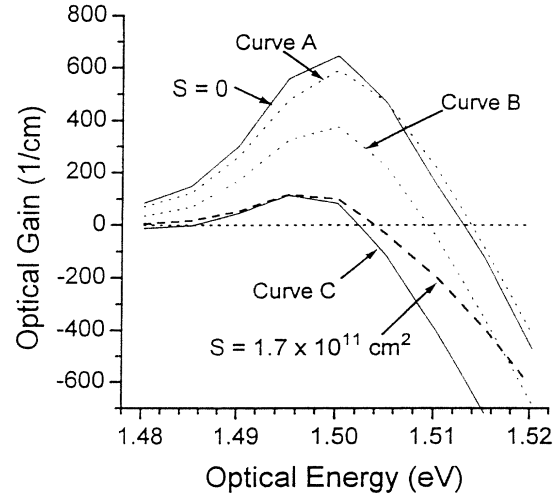


FIG. 8. The optical gain spectra for the two steady-state solutions in the gain saturation simulation. Also shown are the optical gain spectra for (two) steady-state solutions calculated using the quasi-Fermi function. Curves A and B are for the Fermi-based initial and final steady states, respectively. Curve C, based on the quasi-Fermi distribution, has the same peak gain as the dashed curve.

may then be easily calculated from Eq. (32). The numerical value is found to be $\epsilon = 1.1 \times 10^{-17} \text{ cm}^3$ for the 50-Å L-GRINSCH laser structure. This result is comparable with the conclusions of recent experimental studies of subpicosecond gain dynamics in $\text{Al}_x\text{Ga}_{1-x}\text{As}$ laser diodes⁴² and measurements of the intensity modulation spectra of current-modulated Fabry-Pérot lasers.⁴³ Knowing the value of the nonlinear gain coefficient in quantum wells, we can in principle evaluate the maximum modulation bandwidth for the particular design of the quantum-well laser. However, while such a calculation is of considerable importance for quantum-well laser engineering, the final value of the modulation bandwidth does not represent a fundamental quantity directly reflecting the dynamics of carrier thermalization in laser structures. This is largely due to the dependence of the modulation bandwidth on a wide range of system parameters both intrinsic, such as the detailed band structure of the active medium material reflecting in the differential gain, and extrinsic, such as the design of the laser cavity, in particular, the cavity length. Nevertheless, we perform a calculation of the modulation bandwidth for a particular quantum-well laser in order to provide an estimate of small-signal modulation frequencies which are theoretically capable of being achieved (in practical diodes, extrinsic limitations may prevent their achievement). The maximum intrinsic direct-modulation -3-dB bandwidth may be calculated using the small-signal analysis of the semiconductor laser rate equations including the nonlinear gain term.⁴⁴ The resulting value of $f_{\max} = 2^{3/2}\pi/K$, where $K = 4\pi^2[\tau_p + \epsilon/(v_g dg/dn)]$, can be found numerically once the photon lifetime is determined. In a laser with a cavity length of 100 μm having a photon lifetime of $\tau_p = 1.0 \text{ ps}$, a maximum bandwidth of

TABLE I. The 2D and the 3D threshold carrier density n_{th} of the L-GRINSCH quantum-well lasers.

| Well width Å | 40 | 50 | 70 | 100 |
|---|------|------|------|------|
| 2D n_{th} (10^{12} cm^{-2}) | 1.09 | 1.10 | 1.16 | 1.30 |
| 3D n_{th} (10^{18} cm^{-3}) | 2.74 | 2.20 | 1.65 | 1.30 |

78 GHz has been calculated. To achieve the predicted bandwidth, however, the laser has to be biased at a very high optical power (≈ 100 mW) causing detrimental effects of device heating and facet degradation. It is necessary, therefore, to explore injection schemes which will eliminate or reduce gain compression and lower the optical power.

B. Carrier thermalization in quantum wires

The polar optical-phonon scattering rate is shown in Fig. 9 as a function of the initial energy for the case of

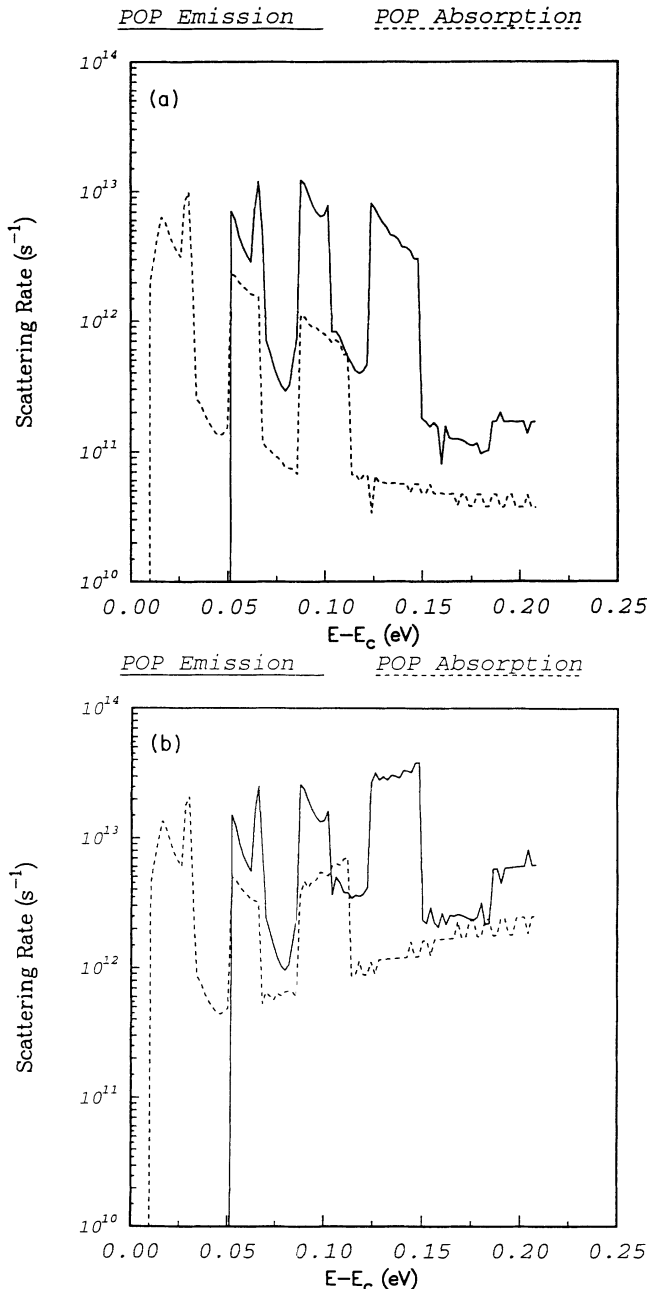


FIG. 9. The polar optical-phonon emission and absorption rates in the $200 \times 200 \text{ \AA}^2$ quantum wire as a function of the initial electron energy for a carrier density of (a) 10^{16} cm^{-3} and (b) 10^{18} cm^{-3} in the wire region.

negligible screening (low injection, $n = 10^{16} \text{ cm}^{-3}$) [Fig. 9(a)] and strong screening (high injection, $n = 10^{18} \text{ cm}^{-3}$) [Fig. 9(b)] in the $200 \times 200 \text{ \AA}^2$ GaAs/ $\text{Al}_{0.3}\text{Ga}_{0.7}\text{As}$ quantum wire. The energy dependence of the scattering rate may be attributed to its dependence on the density of states function and on the matrix overlap element. When the interaction between electrons and polar optical phonons is screened by a high density of intervening charge, necessary to achieve and sustain population inversion in a semiconductor laser, the scattering rate is noticeably reduced in comparison with that in the case of negligible screening. The polar optical emission rate exceeds polar optical absorption rate, ensuring eventual carrier thermalization. At lower temperatures, phonon freezeout makes carrier thermalization considerably more efficient since less phonon absorption occurs.

Our Monte Carlo simulation shows that intersubband electron-electron scattering in the $100 \times 100 \text{ \AA}^2$, in which only two subband energies are below the conduction-band discontinuity is much less efficient than polar optical-phonon scattering and may be neglected with little loss of precision. Instead, relative prominence is gained by inelastic acoustic-phonon and electron-hole scattering processes. The electron-hole scattering rate in quantum wires may be estimated by making the parabolic band approximation in the valence band (neglecting coupling between the states of distinct angular momentum) and assuming that the hole-phonon coupling is strong enough to ensure that the hole distribution is in thermal equilibrium with the lattice at all times. The resulting scattering rate is shown as a function of initial electron energy (summed over all final electron, initial and final hole states) in Fig. 10. The effect of screening on the

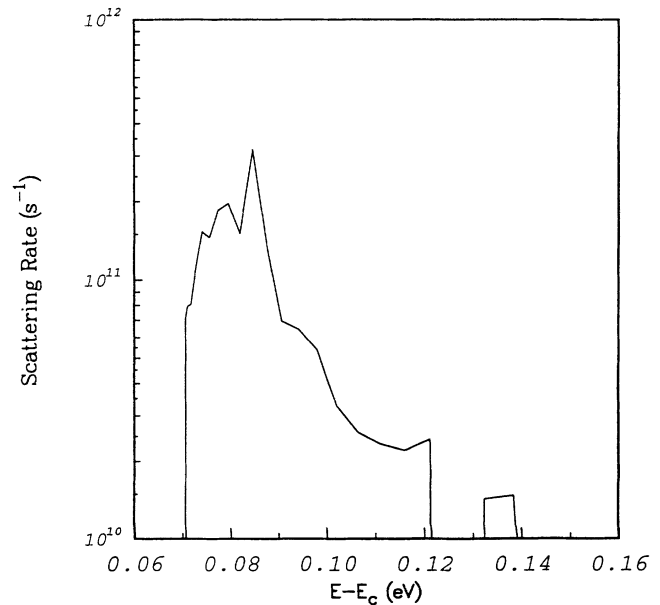


FIG. 10. The electron-hole scattering rate for the $100 \times 100 \text{ \AA}^2$ wire with a carrier concentration of 10^{18} cm^{-3} as a function of the initial electron energy summed over all final electron, initial and final hole states.

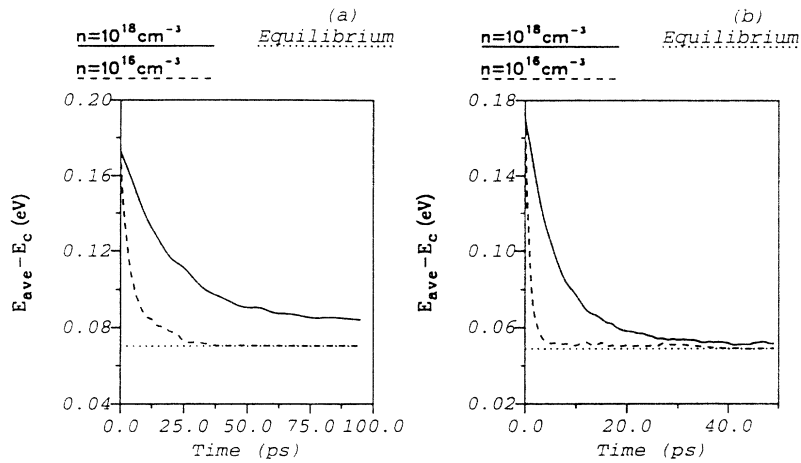


FIG. 11. The time evolution of the mean energy of the electron distribution for (a) $100 \times 100 \text{ \AA}^2$ and (b) $200 \times 200 \text{ \AA}^2$ quantum wires *neglecting* the effects of electron-hole coupling.

electron-hole scattering rate may be estimated in the Thomas-Fermi approximation. Since the hole distribution is assumed to be in static equilibrium, electron-hole scattering actually leads to energy loss for the electron distribution. This energy loss represents the effect of indirect coupling of the electrons to the thermal bath of the lattice mediated by the holes. In view of the simple assumptions adopted above, this energy loss is necessarily overestimated in our simulation apart from the assumption of the static nature of screening, which may cause the strength of the electron-hole interaction to be somewhat underestimated. In this paper, however, we do not aim to obtain a complete description of electron-hole scattering in quantum wires, but rather to provide an estimate of its importance in the relaxation phenomena.

Now we consider the time evolution of the electron distribution as derived from the Monte Carlo simulation. The mean energy of an ensemble of 5000 electrons is shown in Fig. 11 *neglecting* electron-hole scattering processes. The time evolution of the average electron energy can be divided into two periods: (i) fast relaxation primarily by emission of polar optical phonons with a density-dependent characteristic time of a few picoseconds and (ii) slower relaxation primarily by emission of inelastic acoustic phonons for those carriers whose initial energy does not match the average thermal energy plus an integral number of optical-phonon energies. The effect of screening is to slow down relaxation by phonon emission, but if the carrier-carrier scattering rates are properly included, the division between relaxation by emission of optical and acoustic phonons is blurred and carrier thermalization times are closer to those at low carrier densities.

For the $100 \times 100 \text{ \AA}$ wire, in the presence of strong screening, the electron relaxation time exceeds 100 ps, while for the case of negligible screening it is estimated to be ≈ 20 ps. In the $200 \times 200 \text{ \AA}$ wire, the relaxation times are, respectively, 30 and 5 ps. The magnitude of the fluctuations observable in the plots of the mean energy as a function of time after injection can be reduced by increasing the number of simulated electrons. The time evolution of the mean energy of the electron distribution is

given in Fig. 12 *including* electron-hole coupling. The relaxation time is reduced to ≈ 50 ps. Although the loss of energy to the hole distribution by electrons is calculated to be quite high in our model, we would like to point out that this relaxation time is still significantly greater than those calculated for quantum-well structures.

The evolution of the electron distribution as a function of time is presented in Fig. 13. The shape of the distribution function is qualitatively similar in situations with strong and weak screening. The difference is rather in the time scale for electron relaxation as reflected in the time evolution of the mean energy of the electron distribution. The injected distribution is shown as a plot of the

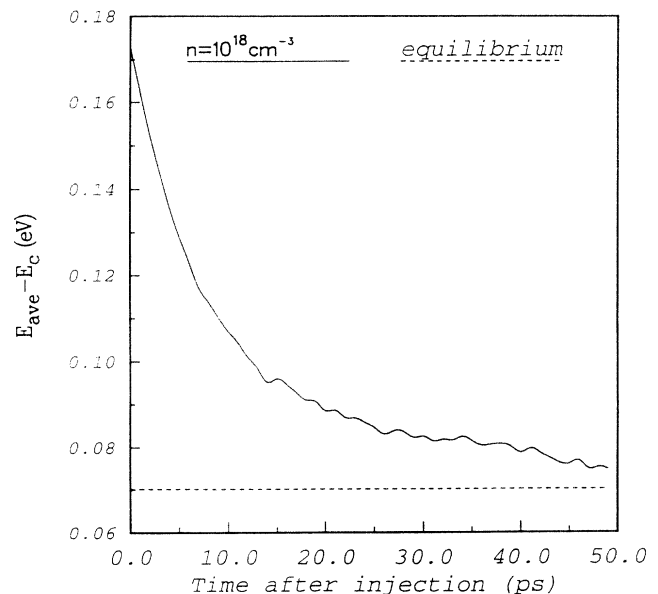


FIG. 12. The time evolution of the mean energy of the electron distribution for the $100 \times 100 \text{ \AA}^2$ quantum wire *including* the effects of electron-hole coupling.

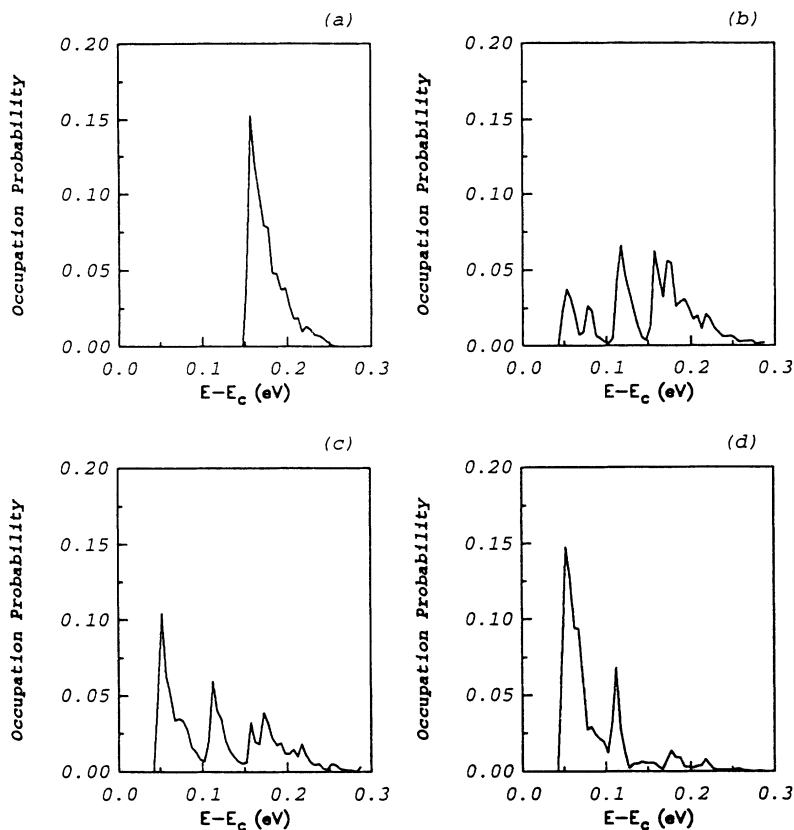


FIG. 13. The time evolution of the electron distribution function for the $100 \times 100 \text{ \AA}^2$ quantum wire for a carrier concentration of 10^{16} cm^{-3} in the wire region. The distribution is shown at (a) injection, (b) 1 ps, (c) 3 ps, and (d) 10 ps after injection.

occupation probability summed over an energy interval of 5 meV. The distribution function is shown at the time of injection and for a number of relevant times after injection. It is found slowly to approach the Boltzmann distribution function with the passage of time. The peaks in the distribution function formed at the subband-edge energies reflect the bottlenecks in carrier relaxation encountered in intersubband transitions. The results for a range of quantum-wire cross sections are summarized in Fig. 14 for quantum wires of square cross sections (an assumption made to simplify the calculations). Since the equilibration process is closely related to the resolution of the bottleneck in phase space occupation, the relaxation time shows a clear dependence on the wire cross section: for larger areas, a greater number of subbands allows more efficient randomization of the electron distribution.

In order to evaluate the effect of a finite intraband relaxation time on the spectral hole burning in quantum wires, we solved the Boltzmann equation by the Monte Carlo technique discussed previously. The steady-state distribution function for a characteristic time of 10 ps is shown in Fig. 15. The effect of injection and extraction terms on the distribution function is seen to be twofold: (i) a spectral hole is burned around the lasing wavelength and (ii) the effective temperature of the electron gas is slightly raised. The reduction in the occupation probability at the lasing wavelength corresponds to the reduction of the optical gain of the lasing mode. The dependence of the reduction in occupation probability on the characteristic injection time is shown in Fig. 16. On the basis of the results presented here, it is clear that the nonlinear

gain coefficient in quantum wires may be increased by a few times in comparison with the coefficient calculated for quantum wells. However, it is difficult to translate the enhancement in the gain compression parameter directly into the reduction in modulation bandwidth. It has been shown that the differential gain in quantum-wire

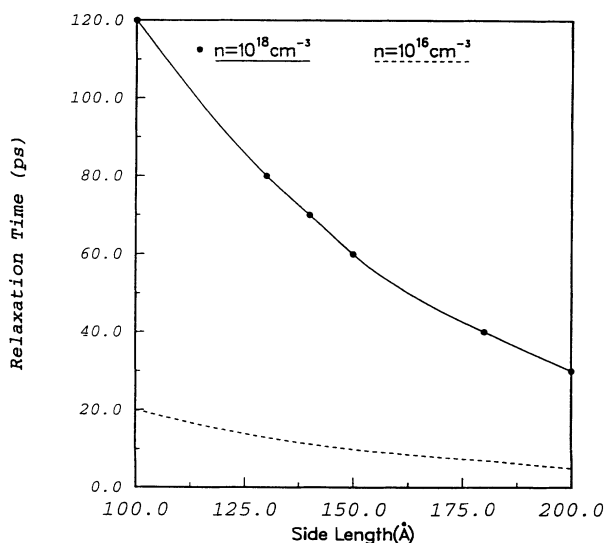


FIG. 14. The electron relaxation time as a function of the wire cross-sectional area. A square cross section is assumed and the length of the side of the square is given as the parameter for carrier concentrations of 10^{16} and 10^{18} cm^{-3} .

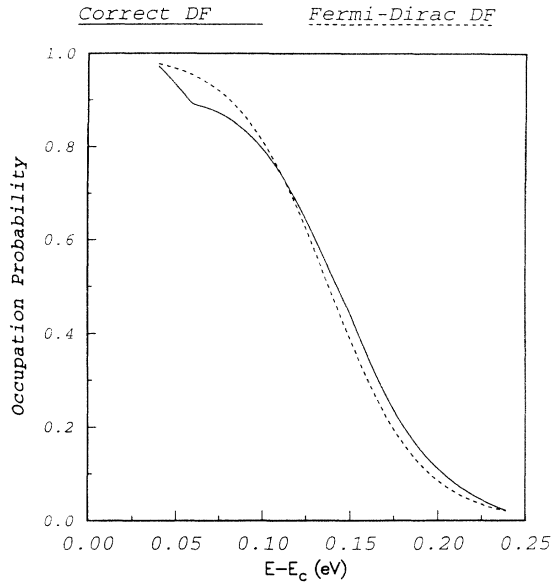


FIG. 15. The distribution function in the presence of spectral hole burning is compared to the equilibrium Fermi-Dirac function for a characteristic extraction time of 10 ps.

laser structures may be as much as an order of magnitude greater than in quantum wells. Nevertheless, it is too simplistic to assume that the differential gain remains unaffected by gain compression, specifically, because the carrier density necessary to overcome the cavity losses changes considerably with the output power for a sufficiently large nonlinear gain coefficient. The most straightforward application of the single-mode equation formalism becomes progressively worse as gain compression

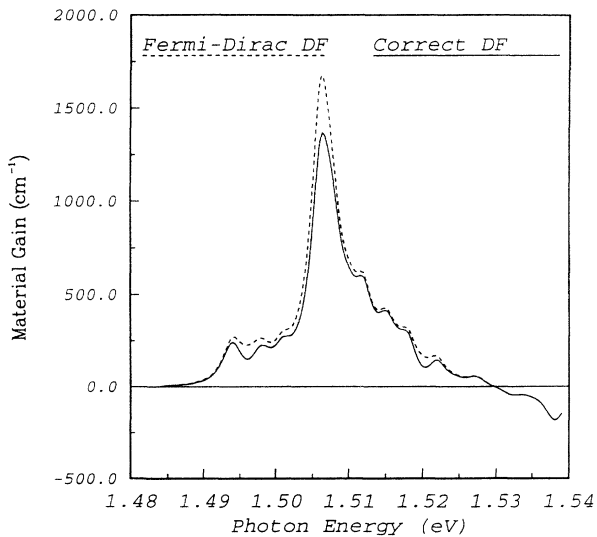


FIG. 16. Peak reduction in the occupation probability at the lasing wavelength as a function of the characteristic extraction time.

is more palpable. The approximation of single-mode constant-wavelength operation and the characterization of the complicated dynamics of carrier relaxation in the presence of very intense stimulated emission in terms of a single constant (nonlinear gain coefficient) begin to break down. The situation is complicated by the fact the practical designs of quantum wire lasers, in glaring contrast with quantum-well lasers, have not been realized. This makes the determination of a parameter such as the modulation bandwidth, dependent on the wide variety of quantities unrelated to the carrier thermalization problem, in our view, premature.

C. Carrier thermalization in quantum dots

Carrier thermalization in quantum dots is conceptually different from carrier thermalization in other low-dimensional electronic systems because a continuum of energies is no longer available to electrons.⁴⁵ Thus attempts to estimate the scattering rates in the same fashion as in other structures are bound to be inaccurate unless the broadening of the energy levels is taken into account. This broadening may arise from a variety of sources such as interface imperfections etc. Here we consider electron thermalization in perfect dots with 3D confinement. Therefore, the broadening of the energy levels can be determined by finding the level lifetime given by the imaginary part of the electron self-energy. The latter is proportional to the scattering rate. Therefore, in order to determine the carrier scattering rates in quantum dots, it is necessary to achieve mutually consistent values of the scattering rates and the broadening of the energy levels induced by scattering. This type of calculation must be performed numerically by iteration on the broadening linewidth.

Even with the inclusion of the broadening levels, it may be conjectured that polar optical-phonon scattering is not very efficient since large deviations from the optical-phonon energy are still unlikely. By performing a Monte Carlo simulation of the relaxation process with self-consistently calculated scattering rates, we find that inclusion of electron-hole scattering can decrease the thermalization time by as much as an order of magnitude. In Fig. 17 the evolution of the mean energy of the electron distribution in the $50 \times 250 \times 250 \text{ \AA}^3$ GaAs/ $\text{Al}_{0.3}\text{Ga}_{0.7}\text{As}$ quantum dot at 300 K is shown with and without electron-hole scattering. In the absence of electron-hole scattering, the relaxation time of several nanoseconds can potentially exceed the nonradiative recombination time. This has been thought to reduce the likelihood of observing photoluminescence from quantum-dot structures.⁴⁶ Several scattering mechanisms have subsequently been examined in order to clarify the relaxation process in quantum dots. While Auger interactions with a dense electron-hole plasma outside of the confined region⁴⁷ require very high concentrations in order to give reasonable relaxation rates, and multiphonon scattering⁴⁸ is a second-order process whose probability is significantly less than that of a first-order process, the mechanism of carrier thermalization in quantum dots suggested here is a first-order process involving carriers

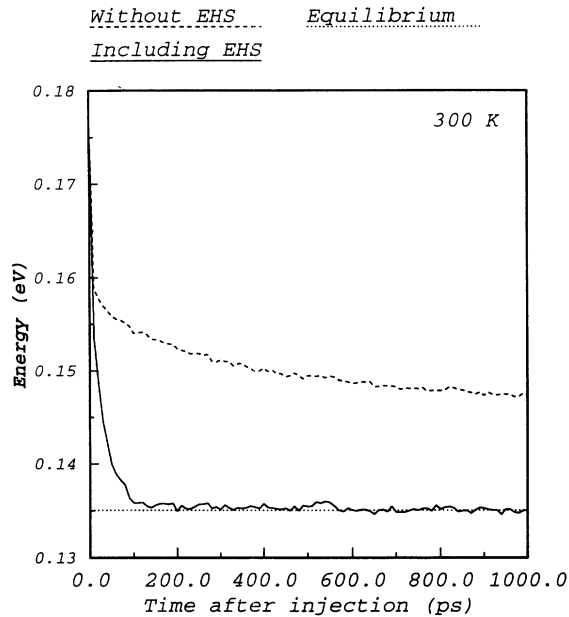


FIG. 17. The mean electron energy as a function of time after injection for the $50 \times 250 \times 250 \text{ \AA}$ GaAs/ $\text{Al}_{0.3}\text{Ga}_{0.7}\text{As}$ quantum dot at 300 K. The horizontal line represents the equilibrium mean energy.

confined in the same (small) volume. On the basis of our results, carrier relaxation is less likely to be the cause of poor luminescence, although the results for very small dots may be affected by the simple assumptions on the hole distribution made in order to evaluate the electron-hole scattering rate.

The carrier thermalization time in quantum dots can thus be estimated to be of the order of several hundred picoseconds depending on the dot size. These times are considerably in excess of the times found for quantum-well and -wire structures. Thus the modulation bandwidth of quantum-dot lasers can be expected not to exceed several gigahertz. The probability of realization of quantum-dot lasers depends critically, however, on the ability to grow 3D arrays of dots with good interface quality. Even if this objective can be achieved, the modulation bandwidth will be intrinsically limited to a value substantially lower than those currently achieved in semiconductor lasers.

IV. CONCLUSIONS

A comprehensive treatment of carrier thermalization in conditions relevant to semiconductor laser operation in structures with quantum confinement of carriers has been presented. We have illustrated the dependence of the thermalization process on the degrees of freedom in quantum wells, wires, and dots, attempting to elucidate the physical peculiarities of the relaxation process. In particular, the reduction in the available final momentum space causes bottlenecks in carrier thermalization which increase the effective time in which thermal equilibrium with the lattice is achieved. When quantum confinement

is realized in all three spatial dimensions, the physics of the relaxation process acquires qualitatively new features. It becomes important to account correctly for the renormalization of the electronic states in the quantum dot occurring as a result of coupling to the phonon bath. Since recently the primary application of quantum structures with confinement in multiple dimensions has been in semiconductor lasers, it is also imperative to include the interactions of the electrons and holes injected into the active region. It has been shown that the relaxation of the carrier type with a time constant much greater than that of the other type (in the absence of the intraband intercarrier interaction) may be significantly speeded up. Because the electron density of states is normally much smaller than the hole density of states, the rate of energy loss to the lattice for holes tends to be much greater than that for electrons. If the electron-hole energy exchange is sufficiently large, however, the electrons are able to couple to the phonon bath indirectly. This type of interaction has been shown to be critical in quantum-dots structures, in which other types of interactions result in a very low energy loss rate.

The electron relaxation time has been found to increase with confinement in further directions. This corresponds to the intuitive expectation based on the reduction in the degrees of freedom associated with the final momentum space. While the thermalization times in bulk materials have been estimated not to exceed 1 ps (in the situation of injection from the cladding layer, spatial diffusion dominates intraband relaxation), we find that the corresponding value in quantum-well systems is of the order of 10 ps. Performing a Monte Carlo simulation, we have established that the major portion of the so-called capture time from the 3D region into the quantum well is spent in transitions between the subbands owing to suppression of intersubband scattering rates. The situation in quantum wires is analogous. We found that in order to obtain a faithful picture of electron relaxation in quantum wires, it is necessary to include the effect of electron-hole scattering since electron-electron scattering in small-area quantum wires is negligible. The calculated relaxation times range from 50 to 100 ps. The relaxation times are increased to several hundred picoseconds in quantum dots.

The intraband relaxation time affects one parameter that is of great interest for semiconductor laser operation—the nonlinear gain coefficient. While, in the steady state, the effect of nonlinear gain is to introduce a small correction to the light-current characteristic at high injected currents, the consequences of gain compression on the dynamics of laser diodes can be quite dramatic. Along with the details of the band structure as expressed in terms of the differential gain, the gain compression coefficient sets the intrinsic upper limit on the modulation bandwidth of the semiconductor laser. We have obtained an estimate of the bandwidth for widely used quantum well lasers of $\approx 80 \text{ GHz}$ for a cavity length of $100 \text{ }\mu\text{m}$, which means that fairly high speeds can be achieved in appropriately designed quantum-well lasers in spite of the increased thermalization time. Moreover, the modulation bandwidth has not been found to scale exactly with the thermalization time, primarily

owing to the variety of parameters on which the former depends. Qualitative estimates of the modulation bandwidth for quantum wires and dots are difficult also because practical laser structures using these structures as active regions have not yet been demonstrated. In general, the evaluation of the modulation bandwidth for significant gain compression may involve reconsidering the single-mode approximation as well as the approximation of dealing with the entire gain compression problem in semiconductor lasers in terms of a single constant non-

linear gain coefficient. Methods of addressing this problem are currently being explored.

ACKNOWLEDGMENTS

Valuable discussions with Dr. J. Hinckley are appreciated. This work was supported by the Army Research Office under Contract No. DAAL 03-92-G-0109 and the Office of Naval Research under Contract No. N00014-90-J-1831.

- ¹*Quantum Well Lasers*, edited by P. Zory (Academic, New York, 1993).
- ²W. Schaff, P. J. Tasker, M. C. Foisy, and L. F. Eastman, in *Semiconductors and Semimetals*, edited by T. P. Pearsall (Academic, San Diego, 1991), Vol. 3, Chap. 2.
- ³E. Yablonivitch and E. O. Kane, *J. Lightwave Technol.* **LT-4**, 504 (1986).
- ⁴Y. Arakawa and H. Sakaki, *Appl. Phys. Lett.* **40**, 939 (1982).
- ⁵Y. Arakawa, K. Vahala, and A. Yariv, *Appl. Phys. Lett.* **45**, 950 (1984).
- ⁶H. C. Casey and M. B. Panish, *Heterostructure Lasers* (Academic, San Diego, 1978).
- ⁷G. P. Agrawal and N. K. Dutta, *Long-Wavelength Semiconductor Lasers* (Van Nostrand Reinhold, New York, 1986).
- ⁸M. Asada and Y. Suematsu, *IEEE J. Quantum Electron.* **QE-21**, 434 (1985).
- ⁹G. P. Agrawal, *IEEE J. Quantum Electron.* **QE-23**, 860 (1987).
- ¹⁰J. M. Luttinger and W. Kohn, *Phys. Rev.* **97**, 869 (1955).
- ¹¹K. J. Vahala and P. C. Sercel, *Phys. Rev. Lett.* **65**, 239 (1990).
- ¹²P. C. Sercel and K. J. Vahala, *Phys. Rev. B* **42**, 3690 (1990).
- ¹³H. Fröhlich, H. Pelzer, and S. Zienau, *Philos. Mag.* **41**, 221 (1950).
- ¹⁴K. Yokoyama and K. Hess, *Phys. Rev. B* **31**, 6872 (1985); **33**, 5595 (1986).
- ¹⁵J. Likari and R. Evrard, *Phys. Rev. B* **15**, 2254 (1977).
- ¹⁶J. P. Leburton, *J. Appl. Phys.* **56**, 2850 (1984).
- ¹⁷J. P. Leburton, *Phys. Rev. B* **45**, 11 022 (1992).
- ¹⁸See, e.g., B. K. Ridley, *Quantum Processes in Semiconductors*, 2nd ed. (Oxford University Press, New York, 1988).
- ¹⁹A. Kabasi, D. Chattopadhyay, and C. K. Sarkar, *J. Appl. Phys.* **65**, 1598 (1989).
- ²⁰R. Mickevicius and V. Mitin, *Phys. Rev. B* **48**, 17 184 (1993).
- ²¹C. Jacoboni and P. Lugli, *The Monte Carlo Method for Semiconductor Device Simulation* (Springer, New York, 1989).
- ²²P. Lugli and D. K. Ferry, *Appl. Phys. Lett.* **46**, 594 (1985).
- ²³P. Lugli and D. K. Ferry, *IEEE Trans. Electron. Devices* **ED-32**, 2431 (1985).
- ²⁴S. M. Goodnick and P. Lugli, *Phys. Rev. B* **37**, 2578 (1988).
- ²⁵L. Rota, F. Rossi, S. M. Goodnick, P. Lugli, E. Molinari, and W. Porod, *Phys. Rev. B* **47**, 1632 (1993).
- ²⁶I. Vurgaftman and J. Singh, *Appl. Phys. Lett.* **64**, 232 (1994).
- ²⁷S. M. Goodnick and P. Lugli, *Phys. Rev. B* **38**, 10 135 (1988).
- ²⁸E. D. Siggia and P. C. Kwok, *Phys. Rev. B* **2**, 1024 (1970).
- ²⁹J. P. Loehr and J. Singh, *IEEE J. Quantum Electron.* **QE-27**, 708 (1991).
- ³⁰Y. Lam and J. Singh, *Appl. Phys. Lett.* **63**, 1874 (1993).
- ³¹Y. Lam and J. Singh, *IEEE J. Quantum Electron.* **QE-30**, 1196 (1994).
- ³²Y. Lam, J. P. Loehr, and J. Singh, *IEEE J. Quantum Electron.* **28**, 1248 (1992).
- ³³K. Henneberger, F. Herzel, S. W. Koch, R. Binder, A. E. Paul, and D. Scott, *Phys. Rev. A* **45**, 1853 (1992).
- ³⁴M. Sargent III, M. O. Scully, and W. E. Lamb, Jr., *Laser Physics* (Addison-Wesley, Reading, MA, 1974).
- ³⁵M. Willatzen, A. Uskov, J. Mørk, H. Olesen, B. Tromborg, and A.-P. Jauho, *IEEE Photon. Techn. Lett.* **3**, 606 (1992).
- ³⁶B. N. Gomatom and A. P. DeFonzo, *IEEE J. Quantum Electron.* **QE-26**, 1689 (1990).
- ³⁷I. Vurgaftman and J. Singh, *J. Appl. Phys.* **74**, 6451 (1993).
- ³⁸S. Morin, B. Deveaud, F. Clerot, K. Fujiwara, and K. Mitsu-naga, *IEEE J. Quantum. Electron.* **QE-27**, 1669 (1991).
- ³⁹J. A. Brum and G. Bastard, *Phys. Rev. B* **33**, 1420 (1986); J. A. Brum, T. Weil, J. Nagle, and B. Vinter, *ibid.* **34**, 2381 (1986).
- ⁴⁰S. Weiss, J. M. Weisenfeld, D. S. Chemla, G. Raybon, G. Suchla, M. Wegener, G. Eisenstein, C. A. Burrus, A. G. Dentai, U. Koren, B. I. Miller, H. Temkin, R. A. Logan, and T. Tanbun-Ek, *Appl. Phys. Lett.* **60**, 9 (1992).
- ⁴¹B. Deveaud, in *Proceedings of the 20th International Conference on the Physics of Semiconductors, Thessaloniki, Greece*, edited by E. M. Anastassakis and J. D. Joannopoulos (World Scientific, Singapore, 1990), p. 1201.
- ⁴²M. P. Kesler and E. P. Ippen, *Appl. Phys. Lett.* **51**, 1765 (1987).
- ⁴³R. Frankenberger and R. Schimpe, *Appl. Phys. Lett.* **57**, 2520 (1990).
- ⁴⁴R. Olshansky, P. Hill, V. Lanzisera, and W. Powazinik, *IEEE J. Quantum Electron* **QE-23**, 1410 (1987).
- ⁴⁵U. Bockelmann and G. Bastard, *Phys. Rev. B* **42**, 8947 (1990).
- ⁴⁶H. Benisty, C. M. Sotomayor-Torres, and C. Weisbuch, *Phys. Rev. B* **44**, 10 945 (1991).
- ⁴⁷U. Bockelmann and T. Egeler, *Phys. Rev. B* **46**, 15 574 (1992).
- ⁴⁸T. Inoshita and H. Sakaki, *Phys. Rev. B* **46**, 7260 (1992).